Bubble Size Estimation in Slurry Bubble Columns from Pressure Fluctuations

V. P. Chilekar, M. J. F. Warnier, J. van der Schaaf, B. F. M. Kuster, and J. C. Schouten
Laboratory of Chemical Reactor Engineering, Eindhoven University of Technology, 5600 MB Eindhoven, The Netherlands

J. R. van Ommen
Reactor and Catalysis Engineering, Delft University of Technology, Julianalaan 136, 2628 BL, The Netherlands

DOI 10.1002/aic.10427
Published online May 2, 2005 in Wiley InterScience (www.interscience.wiley.com).

The average large gas bubble size in slurry bubble columns is estimated using a spectral analysis method applied to measured pressure time series. A pressure time series measured in a bubble column consists of local pressure fluctuations and global pressure fluctuations. The local pressure fluctuations arise from the liquid velocity fluctuations induced by the large gas bubbles and by the changes in gas holdup. The standard deviation of these local pressure fluctuations is a measure of the average large bubble size. The coherence between the pressure time series measured at the sparger and at any other location in the column is used to separate the local pressure fluctuations from the global pressure fluctuations. The global pressure fluctuations are measured instantaneously throughout the column and form the coherent part of the pressure time series. The local pressure fluctuations, which are absent at the sparger, form the incoherent part of the pressure time series. In a 2-D bubble column, a clear correlation is demonstrated between the incoherent standard deviation of the pressure time series and the average large gas bubble size obtained from video imaging. A good agreement is also found between this correlation and the 3-D model proposed by Krishna et al. for predicting the average large bubble size in 3-D (slurry) bubble columns. © 2005 American Institute of Chemical Engineers *AIChE J,* 51: 1924–1937, 2005
Keywords: slurry bubble column, bubble size, pressure fluctuations, Fourier analysis, incoherent standard deviation

Introduction

Slurry bubble columns (SBCs) find a wide range of applications in the chemical process industry because of their simple operation and good heat and mass transfer characteristics. Extensive research has been carried out in the last few decades, to understand both hydrodynamics and mass transfer in (slurry) bubble columns. The effect of several types of solids, liquids, gases, physical properties of fluids, column diameter, distributor design, and so forth, has been carefully studied and summarized.[1-4] However, the design and scale-up of an SBC reactor still remains a troublesome task.[5]

Gas holdup, regime transition point, mass transfer coefficient, axial dispersion coefficient, and average bubble diameter constitute a few of the parameters used as a measure of the performance of SBC reactors. The average bubble diameter is one of these important hydrodynamic parameters, which yields information of the gas–liquid interfacial area as well as of the liquid mixing in the column. However, until now it has not been possible to accurately predict the bubble size. Several nonintrusive techniques,[6] such as laser sheeting,[7] radioactive

V. P. Chilekar is also affiliated with Reactor and Catalysis Engineering, Delft University of Technology, Julianalaan, The Netherlands.
Correspondence concerning this article should be addressed to J. C. Schouten at j.c.schouten@tue.nl.

particle tracking,[8,9] and tomography,[10] are being used in the study of SBCs. However, these techniques are expensive and require extensive expertise in both executing the measurement and interpreting the results. Measurements using optical fiber probes or laser Doppler anemometry give a local estimation of the bubble size, whereas ultrasonic methods give an average bubble size and are effective only at lower gas holdup.

Pressure measurements, discussed herein, are relatively simple, inexpensive, nonintrusive, and already available for most SBCs operated in labs, pilot plants, and large (industrial) installations. Wall pressure fluctuations have been used in the previous decade to study the hydrodynamics of gas–liquid systems using different types of analyses, such as spectral analysis, chaos analysis, and wavelet analysis.[11-17] A drawback of pressure measurements is the complexity generated by different pressure sources in the SBC. The challenge is to extract information from pressure time series that is relevant for the (physical) hydrodynamic phenomenon under study.

First, the origin of pressure fluctuations in SBCs is briefly discussed herein, in terms of possible and relevant sources. Next, the spectral analysis is discussed. Fourier analysis is used in this study as a tool to deconvolute the pressure time series into the local (at the measurement position) and global (throughout the whole column) pressure fluctuations. Subsequently, this analysis is applied to a two-dimensional (2-D) SBC and a correlation between the incoherent standard deviation and the average large bubble diameter is determined empirically. This 2-D SBC correlation is finally also applied to pressure time series measured in a three-dimensional (3-D) SBC to estimate the average large bubble diameter and the predictions are compared with the model of Krishna et al.[18]

Pressure Sources in Slurry Bubble Columns

In an SBC, small gas bubbles are introduced at the gas distributor. These small bubbles coalesce and grow in size as they rise in the column. Liquid is dragged along with the bubbles, which results in a global liquid circulation throughout the column. Liquid circulations influence the path of the rising bubbles and also the breakup of bubbles. Bubbles eventually escape the liquid at the surface. All these phenomena generate pressure fluctuations either locally or globally in the column.

The local pressure fluctuations are caused by pressure sources such as liquid velocity fluctuations and gas holdup fluctuations. Rising gas bubbles, large liquid eddies, and liquid turbulence generate these liquid velocity fluctuations. The gas holdup fluctuations are directly related to the passage of large gas bubbles. The global pressure fluctuations are caused by pressure sources such as bubble formation, bubble coalescence, bubble breakup, bubble eruption, oscillations of the gas–liquid suspension,[19] and mechanical vibrations of the column.[20] The local and global sources can be differentiated based on the propagation velocity of the related pressure sources. The pressure fluctuations from local sources travel with the speed of the source and are measured only in the direct vicinity of the source. These pressure fluctuations have a low propagation velocity (<2 m s^{-1}). Global sources generate pressure waves that travel with the velocity of sound in the gas–liquid suspension, which is given by Mallock[21] as

$$c^2 = \frac{P}{\rho_s \varepsilon_g (1 - \varepsilon_g)} \tag{1}$$

where c the velocity of the sound in the gas–liquid suspension, P is the atmospheric pressure, ρ_s is the density of the slurry, and ε_g is the gas holdup. Equation 1 gives minima for velocity of sound at $\varepsilon_g = 0.5$, which is 20 m s^{-1}. The global sources thus have a high propagation velocity (>20 m s^{-1}), and are measured almost instantaneously throughout the column.

The gas bubbles in an SBC are classified into two distinct classes: small bubbles (2–8 mm) and large bubbles (>8 mm).[22] The volume-averaged bubble diameter estimated from the local pressure fluctuations is related to the small and the large bubble classes. The contribution of the small bubbles, however, is negligible compared to that of the large bubbles. These gas bubbles show a distinct axial distribution in size in the column. Small bubbles are present near the sparger up to the equilibrium height above which the large bubbles are dominant. Above this equilibrium height, turbulent flow is completely developed and the bubbles do not grow further in size by coalescence. In the developed turbulent flow, the large bubbles are uniformly distributed along the radius of the column. At any location above the equilibrium height, the average bubble size is constant. Thus the average bubble diameter measured above the equilibrium height can be considered as the representative diameter of the large bubbles present in the column. The pressure time series measured above this height will capture the pressure fluctuations resulting from all the large bubbles passing the vicinity of the sensor and thus will be representative for all the large bubbles rising in the column.

Theoretically, rising bubbles generate most of the local pressure fluctuations, so these local pressure fluctuations can be used to estimate the average bubble diameter of rising bubbles. Davidson and Harrison[23] proposed a correlation for the pressure fluctuation generated by a single rising bubble in an infinite medium, caused by the gas flow field around it in a fluidized bed. This correlation, when translated to SBCs and converted from its radial coordinates into the time domain (see Appendix) for a two-dimensional (2-D) and a 3-D bubble, is given as

$$P_b(t) \propto \rho_s g \frac{d_b^2}{v_b t} \qquad \text{2D bubble}$$

$$P_b(t) \propto \rho_s g \frac{d_b^3}{v_b^2 t^2} \qquad \text{3D bubble} \tag{2}$$

where d_b is the diameter of the bubble and v_b is the rise velocity of the bubble. This rise velocity of the bubble is proportional to the square root of the bubble diameter,[24] that is, $v_b \propto d_b^{0.5}$, and so $P_b(t) \cong d_b^{1.5}$ for a 2-D bubble and $P_b(t) \cong d_b^2$ for a 3-D bubble. The liquid circulations in the SBC also generate local pressure fluctuations as a result of changes in the liquid velocity field[25] influenced by its interaction with the rising bubbles.

Rising bubbles also generate pressure fluctuations at the measurement position because of changes in the static liquid head above the measurement position. These pressure fluctuations are termed as holdup pressure fluctuations. This holdup pressure fluctuation is seen to be proportional to the volume of

the gas bubbles and in turn proportional to the square of the bubble diameter in a 2-D column and to the cube of the bubble diameter in a 3-D column:

$$P_h(t) \propto d_b^2 \qquad \text{2-D bubble}$$

$$P_h(t) \propto d_b^3 \qquad \text{3-D bubble} \tag{3}$$

In summary, the amplitude of the local pressure fluctuation in an SBC is proportional to a certain power of the large bubble diameter. This power is expected to be between 1.5 and 2 for the 2-D large bubbles and between 2 and 3 for the 3-D large bubbles.

Spectral Analysis of Pressure Time Series

Different time series analysis can be employed to characterize the dynamic behavior of multiphase systems.[26] Van der Schaaf et al.[27] developed a technique to extract information related to the average large bubble diameter from the Fourier transform of pressure time series measured simultaneously in a gas–solid fluidized bed at different column positions. On similar grounds, in this article, Fourier analysis is applied to the pressure time series measured at the wall in SBCs. The pressure time series measured at the axial measuring position x, consists of the sum of pressure fluctuations by local and global sources as

$$P_x(t) = P^{glob}(t) + P_x^{loc}(t) \tag{4}$$

Another pressure time series measured simultaneously at axial position y in the column is given as

$$P_y(t) = a_y P^{glob}(t + \Delta t) + P_y^{loc}(t) \tag{5}$$

where a_y is the attenuation of the global fluctuations at position y as compared to position x and Δt is the time lag. The attenuation is the measure of the dampening of the amplitude of the global fluctuations measured at two different locations, and the time lag gives the time shift of a global pressure fluctuation between the two measurement points. In this section, the separation of the local and the global pressure fluctuations in the measured pressure time series using Fourier analysis is mathematically explained.

Fourier transform

The Fourier transform converts the pressure time series from the time domain to the frequency domain as

$$\mathcal{F}_x(f) = \frac{1}{T}\int_0^T P_x(t) e^{-2\pi i f t} dt \tag{6}$$

A recorded pressure time series is discrete in time, with a constant sampling frequency. A discrete Fourier transform (Fast Fourier Transform) algorithm is used to convert this measured pressure time series into the frequency domain. The Fourier transforms of the pressure time series in Eqs. 4 and 5 are

$$\mathcal{F}_x(f) = \mathcal{F}_x^{loc}(f) + \mathcal{F}^{glob}(f) \tag{7}$$

$$\mathcal{F}_y(f) = \mathcal{F}_y^{loc}(f) + a_y \mathcal{F}^{glob}(f) \tag{8}$$

The above equations show that the Fourier transform of a pressure time series is the sum of the separate Fourier transforms of the local pressure fluctuations and the global pressure fluctuations.

Power spectral density

The power spectral density (PSD) of a pressure time series at measuring position x, Φ_{xx}, is defined as

$$\Phi_{xx}(f) = \frac{1}{T} E[\mathcal{F}_x(f) \cdot \mathcal{F}_x^*(f)] \tag{9}$$

where E is the expectation of $\mathcal{F}_x$, $\mathcal{F}_x^*$ is the complex conjugate of the Fourier transform. By applying Eq. 9 to Eq. 7, the PSD of the pressure time series at position x is calculated as

$$\Phi_{xx} = E\{[\mathcal{F}_x^{loc}(f) + \mathcal{F}^{glob}(f)] \cdot [\mathcal{F}_x^{loc}(f) + \mathcal{F}^{glob}(f)]^*\} \tag{10}$$

Simplifying Eq. 10 gives

$$\Phi_{xx}(f) = |\mathcal{F}_x^{loc}(f)|^2 + |\mathcal{F}^{glob}(f)|^2 + 2E[\mathcal{F}_x^{loc}(f) \cdot \mathcal{F}^{glob}(f)]^* \tag{11}$$

The local and global fluctuations are created by different pressure sources as mentioned in the previous section. These pressure fluctuations cannot be cross-correlated with each other in a pressure time series and thus can be assumed independent of each other. Consequently, the product of their Fourier transforms becomes equal to zero. Thus, in Eq. 11, the last term is equated to zero, which gives

$$\Phi_{xx}(f) = |\mathcal{F}_x^{loc}(f)|^2 + |\mathcal{F}^{glob}(f)|^2 \tag{12}$$

Similarly, the PSD at position y is given by

$$\Phi_{yy}(f) = |\mathcal{F}_y^{loc}(f)|^2 + a_y^2 |\mathcal{F}^{glob}(f)|^2 \tag{13}$$

The cross-power spectral density (CSD) between two time series is given as

$$\Phi_{xy}(f) = \frac{1}{T} E[\mathcal{F}_x(f) \cdot \mathcal{F}_y^*(f)] \tag{14}$$

Substituting the Fourier transform of the pressure time series in the above equation gives

$$\Phi_{xy}(f) = E[\mathcal{F}_x^{loc}(f) \cdot \mathcal{F}_y^{loc*}(f)] + E[\mathcal{F}_x^{loc}(f) \cdot a_y \mathcal{F}^{glob*}(f)] + E[\mathcal{F}^{glob}(f) \cdot \mathcal{F}_y^{loc*}(f)] + a_y |\mathcal{F}^{glob}(f)|^2 \tag{15}$$

In Eq. 15, the first three terms are equal to zero because, by definition, the local pressure sources at different measurement

positions are not correlated with each other. At the same time, the local and global pressure sources are also independent of each other as mentioned earlier. Consequently,

$$\Phi_{xy}(f) = a_y|\mathcal{F}^{glob}(f)|^2 \tag{16}$$

Equation 16 shows that the CSD corresponds to the cross-correlation of the two time series. It is a measure of the global pressure fluctuations recorded in the two time series and gives its power over the complete frequency spectrum.

The global pressure fluctuations cannot be simply subtracted between the two pressure time series to obtain the local pressure fluctuations, because of the attenuation of the signal a_y and the time shift Δt, of the same sources in the two signals.[28] The so-called coherence is therefore used to separate the local fluctuations from the global fluctuations.

Coherence

The pressure fluctuations caused by global pressure sources have a high propagation velocity and thus they generate a constant time shift when measured at two different heights in the column. Because of this, they are coherent over the height of the column. Local pressure sources, such as large gas bubbles, undergo a change in shape and velocity as they rise in the column. The time shift from these sources is therefore not constant. Local pressure sources are thus globally incoherent. In gas–solid fluidized beds, this characteristic difference between local and global pressure sources has been used to successfully separate them using the so-called coherence.[27] The coherence is defined as the CSD of the two time series normalized by the PSDs of the individual time series

$$\gamma_{xy}^2(f) = \frac{|\Phi_{xy}(f)|^2}{\Phi_{xx}(f)\Phi_{yy}(f)} \tag{17}$$

A constant phase lag created by a pressure source gives a coherence of unity at its characteristic frequency. If the phase lag is not constant then the coherence is less than unity and its value varies between zero and one. For completely uncorrelated signals the coherence is zero. From Eqs. 12, 13, 16, and 17 the coherence between the two time series x and y is obtained as

$$\gamma_{xy}^2(f) = \frac{a_y^2|\mathcal{F}^{glob}(f)|^4}{[|\mathcal{F}_x^{loc}(f)|^2 + |\mathcal{F}^{glob}(f)|^2][|\mathcal{F}_y^{loc}(f)|^2 + a_y^2|\mathcal{F}^{glob}(f)|^2]} \tag{18}$$

The product of the coherence (between the measurement position and the sparger position) and the PSD (at the measurement position) gives the so-called coherent output power (COP) that is present in the signal at the measurement position. The COP at position y is calculated as

$$\mathrm{COP}_y(f) = \gamma_{xy}^2(f)\Phi_{yy}(f) \tag{19}$$

From Eqs. 13 and 18, the above equation is further simplified as

$$\mathrm{COP}_y(f) = \frac{a_y^2|\mathcal{F}^{glob}(f)|^4}{|\mathcal{F}_x^{loc}(f)|^2 + |\mathcal{F}^{glob}(f)|^2} \tag{20}$$

Equation 20 clearly demonstrates that the local pressure fluctuations at measurement position x influence the COP calculated at the measurement position y. Thus, the measurement position x needs to be chosen such that the local pressure fluctuations at this position are minimum or (almost) absent. This is possible when this pressure measurement is done in the plenum or just above the gas distributor, where large gas bubbles have not yet been formed, while as yet there are also no large liquid velocity fluctuations. With a measurement position x close to the gas distributor, it can be assumed that $|\mathcal{F}_x^{loc}| \approx 0$, and the COP in Eq. 20 is simplified to

$$\mathrm{COP}_y(f) = a_y^2|\mathcal{F}^{glob}(f)|^2 \tag{21}$$

Equation 21 shows that the COP gives the power in the PSD related to the global pressure fluctuations along with its attenuation at that particular measurement position y. The residual power in the PSD is the so-called incoherent output power (IOP). This IOP at the measuring position y is given as

$$\mathrm{IOP}_y(f) = [1 - \gamma_{xy}^2(f)]\Phi_{yy}(f) \tag{22}$$

Simplifying Eq. 22, using Eqs. 16 and 18, gives

$$\mathrm{IOP}_y(f) = |\mathcal{F}_y^{loc}(f)|^2 + a_y^2\frac{|\mathcal{F}_x^{loc}(f)|^2|\mathcal{F}^{glob}(f)|^2}{|\mathcal{F}_x^{loc}(f)|^2 + |\mathcal{F}^{glob}(f)|^2} \tag{23}$$

Simplifying Eq. 23 gives

$$\mathrm{IOP}_y(f) = |\mathcal{F}_y^{loc}(f)|^2$$

$$\text{if} \quad |\mathcal{F}_x^{loc}(f)| \to 0 \quad \text{or} \quad |\mathcal{F}^{glob}(f)| \to 0 \tag{24}$$

Equation 24 shows that the IOP at measurement position y contains only the local pressure fluctuations present in the pressure time series measured at the position y, provided the measurement position x is such that either $\mathcal{F}_x^{loc}$ or $\mathcal{F}^{glob}$ is close to zero, that is, in the plenum or just above the gas distributor.

The above analysis shows that the coherence effectively separates the local pressure fluctuations (IOP) from the global pressure fluctuations (COP) in a measured pressure time series. Parseval's theorem states that the area under the curve of the incoherent output power as a function of frequency is equal to the variance of the incoherent part of the signal, σ_i^2, in the pressure time series

$$\sigma_i^2 = \sum_f \mathrm{IOP}_y(f) \tag{25}$$

This variance is therefore a measure of the power of the pressure fluctuations produced by the rising large bubbles and, as mentioned earlier, is considered to be a function of the average large bubble diameter in the SBC.

Relation between σ_i^2 and d_b

The variance of the pressure fluctuations (σ_p^2), measured in the SBC at any position, is the addition of the variance of the local (incoherent) pressure fluctuations (σ_i^2) at that position and the variance of the global (coherent) pressure fluctuations (σ_c^2)

$$\sigma_p^2 = \sigma_i^2 + \sigma_c^2 \tag{26}$$

σ_i^2 is separated from σ_p^2 using the spectral analysis method as explained in the previous section. σ_i^2 can then be related to the average large bubble diameter as follows

$$\sigma_i^2 = \frac{1}{N}\sum_{n=1}^{N} f_{s,n}\sigma_{s,n}^2 = \frac{1}{T}\sum_{T} |P_b(t)|^2 = \rho_s^2 g^2 f(d_{b,avg}) \tag{27}$$

where s refers to a source of local pressure fluctuation (such as the rising bubble pressure fluctuation, the gas holdup fluctuation, or the liquid velocity fluctuation) and n refers to the different classes of bubble size present. In Eq. 27 each class of bubbles contributes to the incoherent standard deviation σ_i, depending on its own standard deviation and frequency of occurrence of that class of bubbles. In other words, the incoherent standard deviation is the standard deviation of the local pressure fluctuations and is a function of the average large bubble diameter as in Eq. 27. For example, from Eqs. 2 and 3, we can expect in a 3-D SBC that the incoherent standard deviation is proportional to the average large bubble diameter to the power of 2 to 3. This is the basis used for the pressure fluctuations technique explained in this report, that is, $\sigma_i \sim d_b^m$ with $m = 2$ to 3. It is important to mention here that liquid velocity fluctuations are inherently a part of the incoherent pressure fluctuations caused by the rising large gas bubbles. Therefore Eq. 27 also contains the power in the pressure fluctuations resulting from liquid velocity fluctuations along with the rising bubble fluctuations.

Experimentation

The 2-D and 3-D SBCs used in this study are schematically shown in Figure 1. All experiments were carried out with demineralized water and air. A perforated plate sparger was used in both SBCs with 0.5-mm-diameter holes placed in a triangular pitch of 7 mm. The dimensions of the sparger for the 2-D and 3-D SBCs are 200 × 15 × 5 mm (length × breadth × thickness) and 170 × 5 mm (diameter × thickness), with 49 and 550 holes, respectively. The gas flow was controlled by a set of mass flow controllers. Carbon particles of 40 μm were used to prepare the slurry. The carbon particles were prewashed with demineralized water to remove possible contaminations. The particles were mixed with demineralized water and stirred overnight to ensure that the particles are completely wetted during the experiments.

Pressure time series measurement

In both the SBCs, fast dynamic Kistler piezo electric pressure transducers, type 7261, were used to record the pressure time series. Pressure time series were recorded for 30 min at 200 Hz using the SCADAS II system from LMS (Breda, The Netherlands). Bubbles generate pressure fluctuations only up to 50 Hz, as explained later in the results and discussion section; thus the signal was low-pass filtered at 100 Hz during data acquisition. The combined nonlinearity, hysteresis, and repeatability of the Kistler sensor is 0.8% at the full-scale output (2 kPa). The combined error in pressure measurements by the Kistler pressure transducers is thus <2 Pa. In the 2-D column, four pressure transducers were mounted flush to the inner surface of the back wall at heights of 2.5, 48.5, 83.5, and 118.5 cm above the sparger. In the 3-D column, five pressure transducers were mounted flush to the inner surface of the column at heights of 2, 130, 140, 150, and 160 cm above the sparger, as shown in Figure 1.

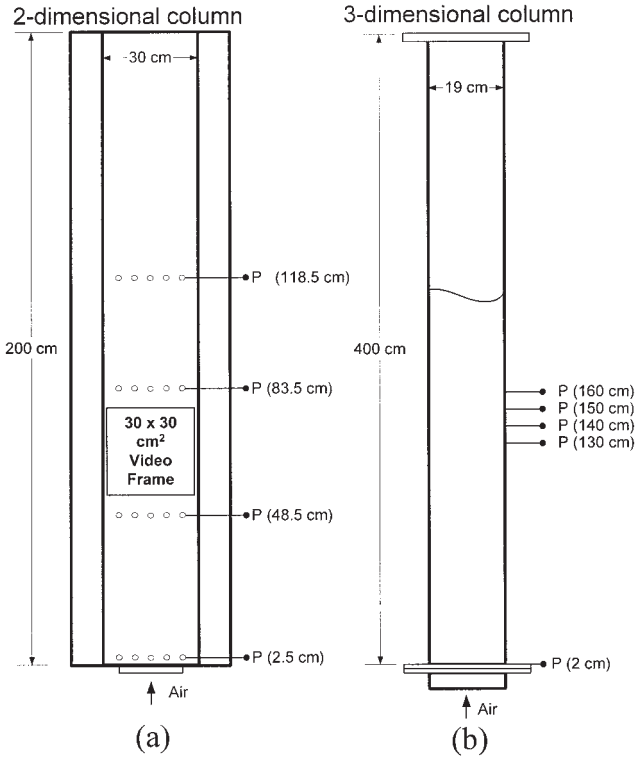

Figure 1. Experimental setups: (a) 2-D SBC: 0.3 × 0.015 × 1.5 m; (b) 3-D SBC: 0.19-m inner diameter and 4 m high.

P is the position of the pressure transducer.

The pressure time series were processed using the available subroutines in Matlab® 6.0 (The MathWorks, Natick, MA). Each pressure time series of 180,000 points was divided into blocks of 1024 points, using an overlap of 50% of the block length and a Hanning window to prevent edge effects. The spectral resolution was 0.195 Hz over the frequency range of 0–100 Hz. Each block was linearly detrended to prevent offset accumulation below the spectral resolution.

High-speed video imaging

Video images were measured using a high-speed Dalsa CA-D6 camera (Tech5 B.V., Hardinxveld-Giessendam, The Netherlands). The video images were recorded between two pressure measurement positions at a height of 48.5 and 83.5 cm for a period of 50 s at a rate of 50 frames/s (fps). The frame

resolution was 256 × 256 pixels corresponding to an area of 0.3 × 0.3 m. The recorded images were processed and analyzed with image processing software developed at our laboratory based on Matlab® 6.0. Bubble size distribution was obtained by processing the captured video images. Details of the video processing are given by Kluytmans.[29]

The distance between the flat plates of the 2-D column is 15 mm, and thus the bubbles with diameter > 15 mm touch both the walls of the column and can be identified as large bubbles by the image-processing software. The large bubble population is assumed to start from the bubble area of 40 pixels (equivalent to a bubble diameter of 8 mm). The bubbles < 40 pixels are recognized as small bubbles. Based on the bubble size classification of Krishna et al.[18] and visual study of video images, these small bubbles (<8 mm) are assumed equal in size. The volume-averaged large bubble diameter $d_{b,avg}$ is defined as

$$d_{b,avg} = \sqrt{\frac{\sum_{n=1}^{N} d_{b,large,n}^2}{\sum_{n=1}^{N} n}} \tag{28}$$

where n is the class of bubble sizes, N is the total number of classes, and $d_{b,large,n}$ is the bubble diameter of the class. At each gas velocity, $d_{b,avg}$ is obtained twice, by processing two movies of 2500 frames, each. Further details of the image-analysis software and the video movies are available on our Web site (http://www.chem.tue.nl/scr).

Results and Discussion

Characteristic frequencies of pressure sources

Single-bubble experiments were conducted in the 2-D SBC to determine the frequency range and amplitudes of the pressure fluctuations generated by rising large gas bubbles. Typical pressure time series measured during the injection and passing of a single large gas bubble are shown in Figure 2. A 0.1-s gas pulse was injected at 0.05 s, which immediately leads to large oscillations. A pressure drop, resulting from the passing of the bubble at the respective pressure sensor positions, is observed at around 1, 2, and 2.75 s. After the bubble passed each sensor, the pressure recovered back to zero. Figure 2 clearly shows that a rising gas bubble generates a pressure fluctuation only in its vicinity. It is observed that large bubbles of 4 to 5 cm generate pressure fluctuations in the range of 2 to 5 Hz.

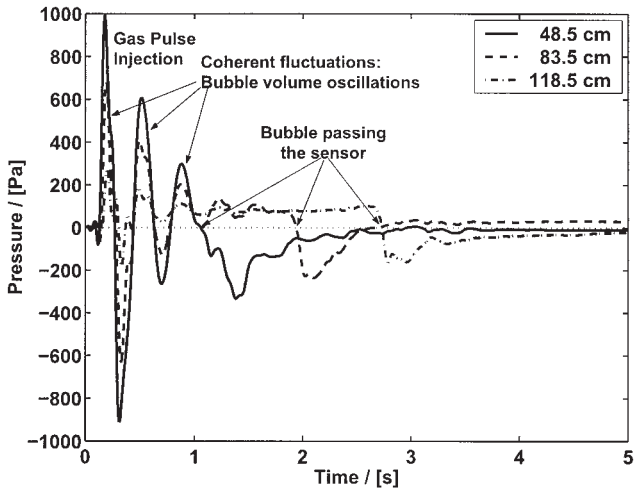

Figure 2. Pressure time series measured at heights of 48.5, 83.5, and 118.5 cm above the sparger in the 2-D SBC for a single pulse of gas bubble.

Gas pulse time = 0.1 s; injection time = 0.5 s; approximate bubble diameter = 5 cm.

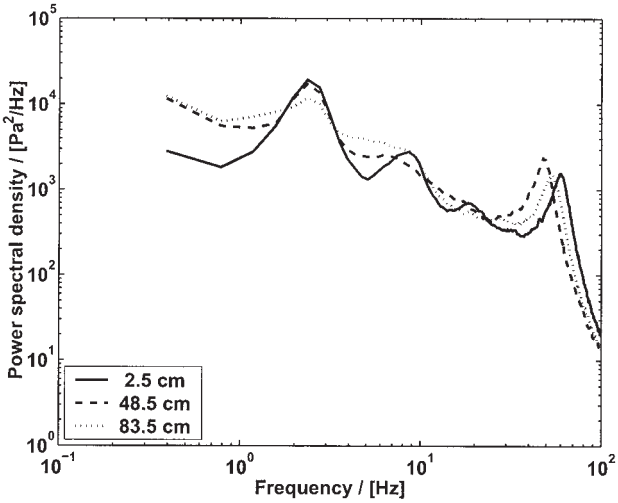

Figure 3. Power spectral density of the pressure time series recorded in the 2-D SBC at different heights of 2.5, 48.5, and 83.5 cm above the sparger at the superficial gas velocity of 0.13 m s^{-1}.

Liquid circulations are developed during uniform bubbling throughout the cross section of the bubble column. These liquid circulations increase the bubble rise velocity. Thus the frequency of pressure fluctuations produced by passing bubbles during uniform bubbling is expected to be higher than that for a single bubble rising in a stagnant liquid. For smaller bubbles of size around 8 mm, the slip velocity between liquid and bubbles is low (~0.2 m s^{-1}) and bubbles travel with a velocity close to the liquid velocity. The passage time of the small bubbles can be calculated based on their rise velocity and size. Small bubbles of around 4 mm can thus generate fluctuations up to 50 Hz. It was observed that bubbles with diameter < 8 mm do not produce significant fluctuations with measurable amplitude. The large bubbles having diameter ranging from 8 mm to 6 cm can generate pressure fluctuations between 2 and 50 Hz depending on their rise velocity and the liquid circulations present. A pressure time series thus measured at 200 Hz and filtered at 100 Hz contains all the pressure fluctuations produced by the rising bubbles.

Power spectral density

Video images and pressure time series were recorded simultaneously during uniform bubbling experiments in the 2-D column. Power spectral densities (PSDs) of pressure time series at measurement positions of 2.5, 48.5, and 83.5 cm height above the sparger for a gas velocity of 0.13 m s^{-1} are shown in Figure 3. At the height of 2.5 cm, very close to the sparger, only small bubbles that generate low power are present. Higher

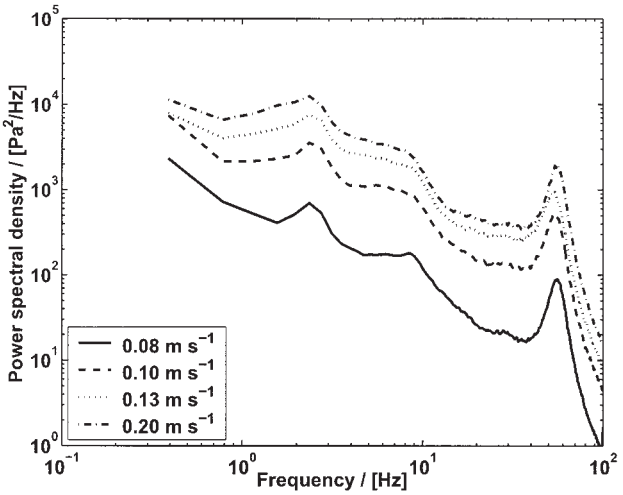

Figure 4. Power spectral density of the pressure time series recorded at gas velocities of 0.08, 0.1, 0.13, and 0.2 m s^{-1} in a 2-D SBC at height of 83.5 cm above the sparger at different superficial gas velocities.

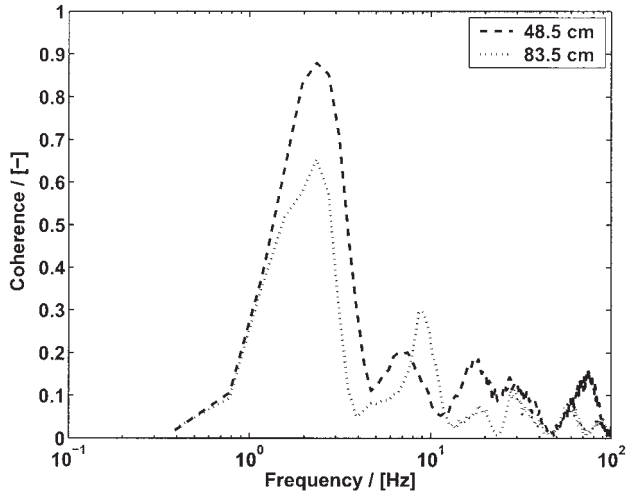

Figure 5. Coherence between the two pressure time series measured at heights of 48.5 and 83.5 cm with the pressure time series measured at the sparger in the 2-D SBC.

The superficial gas velocity is 0.13 m s^{-1}.

in the column large bubbles generate more power, which is seen clearly in Figure 3. PSDs of pressure time series measured at the height of 83.5 cm from the sparger, at different gas velocities, are shown in Figure 4. This figure shows that the overall power is considerably lower at the lower gas velocities. In the homogeneous regime, only small bubbles are present, which rise slowly with a constant velocity and generate low power. The power increases with increasing gas velocity in the heterogeneous regime because of the occurrence of large gas bubbles. No new peaks are observed nor is there any shift in peaks resulting from the presence of the large gas bubbles. Only the total power increases at higher gas velocities.

In the PSDs of Figures 3 and 4, the power is higher at the lower frequencies between 0 and 10 Hz, attributed to the large bubbles generating pressure fluctuations in this frequency range. Above 10 Hz, the power drops rapidly, resulting from the lower amplitude of the pressure fluctuations from the smaller bubbles generating higher frequencies. The peaks around 2 Hz can be attributed to the column mass oscillations arising from the bubble formation phenomena, which also demonstrates a highly coherent peak observed in the coherence spectra[19] (see Figure 3).

Coherence

The coherence of the pressure time series measured at the sparger and at the measurement positions of 48.5 and 83.5 cm, respectively, is shown in Figure 5. A high coherence is observed at frequencies < 5 Hz. These are related to the globally coherent fluctuations, that is, liquid level oscillations and column mass oscillations. The coherence is very low at the higher frequencies from 5 to 50 Hz, which indicates that either the coherent pressure sources do not generate much power at these frequencies or there are very few coherent pressure sources in this range of frequencies. The low coherence beyond 5 Hz can be linked to the local incoherent pressure fluctuations as a result of the rising bubbles and the liquid velocity fluctuations. Thus the coherence directly gives the fraction of the power in the PSDs related to the local and global pressure sources. The coherence between the measurements positions 83.5 and 2.5 cm, at different gas velocities, is given in Figure 6. The amplitude of the high coherent peak at 2.2 Hz does not change with increasing gas velocity. This indicates that as the power in the PSD increases in Figure 4, the coherent and incoherent power increase proportionally, which keeps the coherence constant (Figure 6). There are other peaks observed in Figure 6 at higher frequencies, around 9, 20, 30, 60, and 90 Hz. These are the peaks of lower power and are the harmonics of the high-power peak at 2.2 Hz.

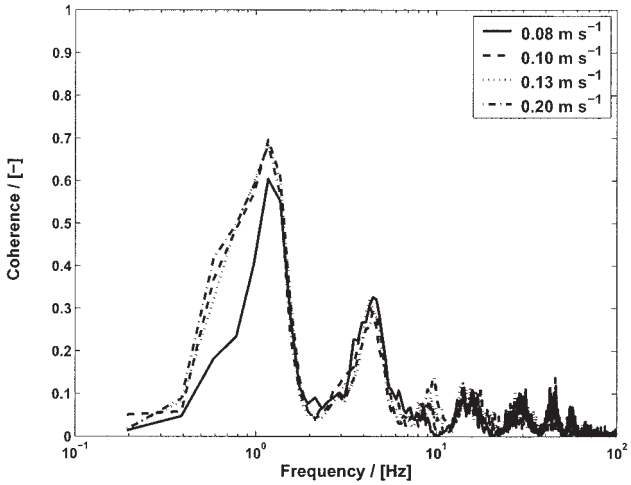

Figure 6. Coherence between the pressure time series recorded at height of 48.5 cm and at the sparger in the 2-D SBC at different superficial gas velocities.

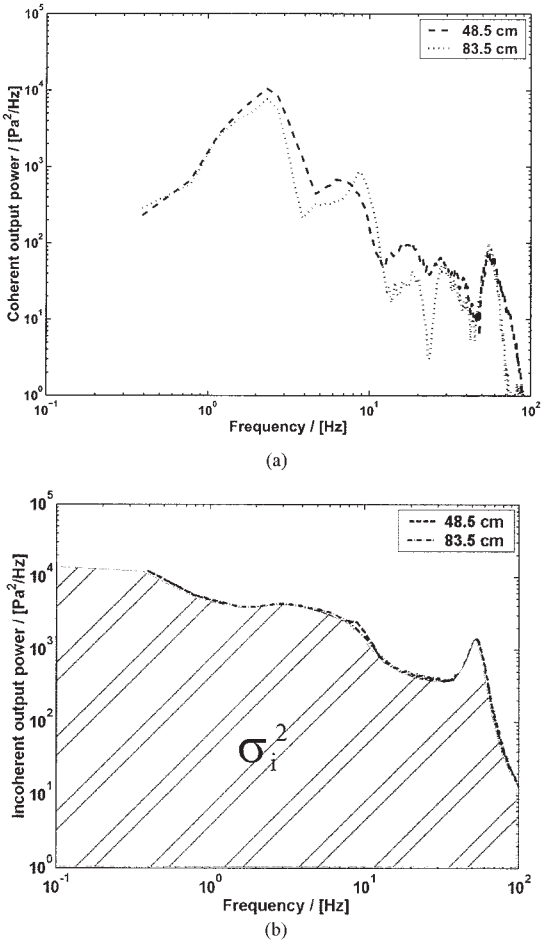

Figure 7. (a) Coherent output power and (b) incoherent output power of the pressure time series at measurement heights of 48.5 and 83.5 cm from the sparger at superficial gas velocity of 0.13 m s^{-1} in the 2-D SBC.

Coherent output power and incoherent output power

The COP and the IOP are calculated from the coherence and PSD using Eqs. 21 and 22, respectively. The COP obtained from the pressure time series at the measurement positions 48.5 and 83.5 cm is shown in Figure 7a. The corresponding IOPs are shown in Figure 7b. Figures 8a and 8b show the COPs and the IOPs at different superficial gas velocities in the heterogeneous regime for the pressure time series measured at 83.5 cm above the sparger. The IOP shows smooth profiles, which drop beyond 10 Hz. The peak near 2.2 Hz observed in all the PSDs (see Figure 4) is clearly present in the COPs in Figure 8a as well, which proves that the peak is attributed to a coherent pressure source such as column mass oscillations. The COP also shows other peaks at higher frequencies, which are similar to the harmonics of the peak at 2.2 Hz. The IOP at frequencies beyond 10 Hz is nearly equal to the PSDs, which indicates that all the power in that region arises from local pressure fluctuations, such as that attributed to small bubbles.

The standard deviation of the incoherent power is calculated from the area under the IOP curves (Eq. 25). This so-called incoherent standard deviation is obtained at the measurement positions of 48.5 and 83.5 cm above the sparger for different superficial gas velocities.

Correlation between σ_i and $d_{b,avg}$

The video images were recorded synchronously with the pressure time series in the 2-D column for a range of gas velocities in the homogeneous and heterogeneous regimes. Two videos, each 50 s long (each video of 2500 frames), were captured after 5 and 25 min of measurement in the total measurement time of 30 min for each gas velocity. Figure 9 shows three representative frames from the video images captured at three different superficial gas velocities in the 2-D SBC. In Figure 10 the bubble size distribution obtained from the video processing is given for all measured superficial gas velocities. The volume-averaged large bubble diameter at each gas velocity was calculated from the bubble size distribution, as shown in Figure 11.

The left frame in Figure 9 shows that at $u_g = 0.07$ m s^{-1} only small bubbles are present in the SBC and the flow is homogeneous. There are very few large bubbles > 8 mm,

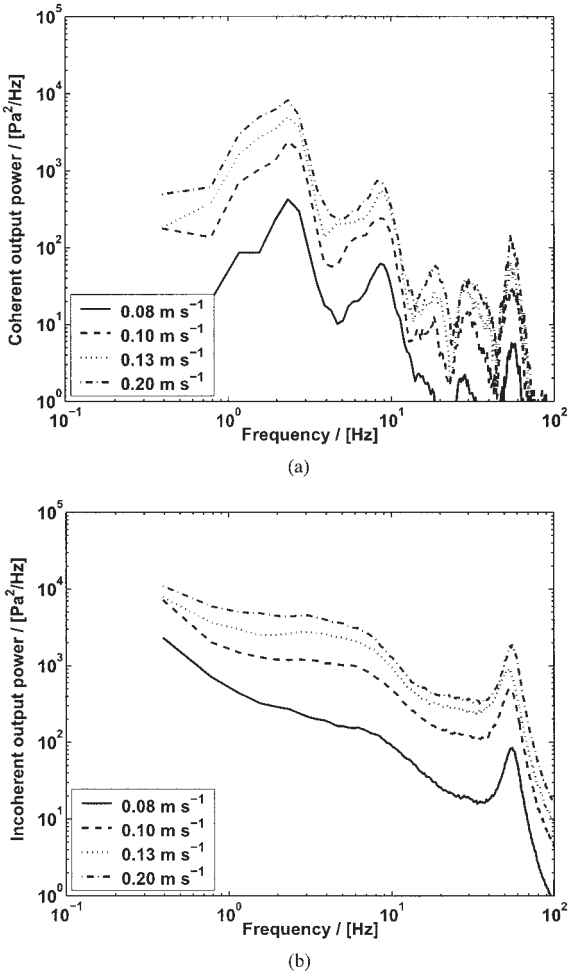

Figure 8. (a) Coherent output power and (b) incoherent output power of the pressure time series at the measurement height of 83.5 cm from the sparger at different superficial gas velocities in the 2-D SBC.

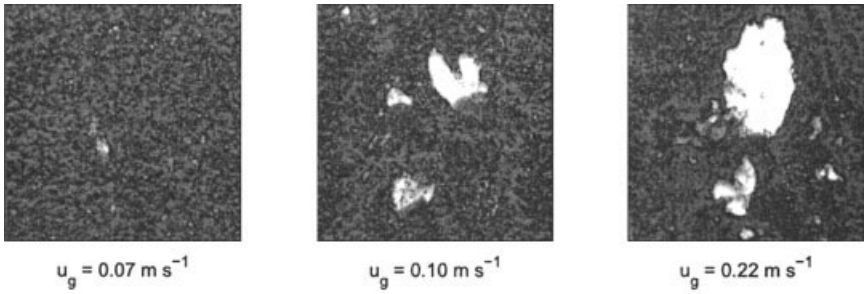

Figure 9. Video images captured in the 2-D column for 0.056 vol/vol % carbon slurry in demineralized water at superficial gas velocities of 0.07, 0.10, and 0.22 m s^{-1}.

meeting the criterion for video processing. The average bubble size is thus <8 mm at these lower superficial gas velocities up to $u_g = 0.07$ m s^{-1}, as in Figure 11. The middle frame in Figure 9 shows the video image captured at $u_g = 0.10$ m s^{-1}. Here few clusters of large bubbles are seen. Around this velocity there is increased bubble coalescence stemming from the transition from the homogeneous flow regime to the heterogeneous flow regime. In the transition regime the average large bubble size increases rapidly with superficial gas velocity, as seen in Figure 11. In the right frame in Figure 9, at $u_g = 0.22$ m s^{-1}, the flow is completely heterogeneous. The heterogeneity leads to larger bubbles that are clearly visible. The average large bubble size in the heterogeneous regime increases slowly as a wide bubble size distribution is obtained as compared to the lower gas velocities (see Figure 10).

The incoherent standard deviation was also obtained in the 2-D SBC at each gas velocity by applying spectral analysis to the pressure time series measured at 48.5 and 83.5 cm above the sparger. In Figure 12, the incoherent standard deviation is plotted against the average large bubble diameter. Based on Eq. 27, a power-law relationship between $\sigma_i/\rho_s g$ and $d_{b,avg}$ was fitted to the experimental data:

$$\frac{\sigma_i}{\rho_s g} = (75.31 \pm 0.51) d_{b,avg}^{(2.300 \pm 0.008)} \quad \text{(m)} \qquad (29)$$

or

$$d_{b,avg} = 0.153 \left(\frac{\sigma_i}{\rho_s g} \right)^{0.434} \quad \text{(m)} \qquad (30)$$

The confidence interval for the fit was 95%. The constant in Eq. 29, 75.31 ± 0.51, contains the influence of the presence of the small bubbles and also of the frequency of occurrence of the large bubbles, which cannot be accounted for as a separate parameter. The power of $d_{b,avg}$ was expected to be between 1.5 and 2 according to Eqs. 2 and 3 for 2-D columns, and between 2 and 3 for 3-D columns. To verify the sensitivity of this power of $d_{b,avg}$, the data were also fitted with $d_{b,avg}$ to the power of 1.5, 2, and 3, leading to different constants in Eq. 29 (see Figure 12). The area between the two curves with $d_{b,avg}^{1.5}$ and $d_{b,avg}^{2}$ is the region where the average bubble diameter in a 2-D column is expected and between the curves of $d_{b,avg}^{2}$ and $d_{b,avg}^{3}$, where the average bubble diameter in 3-D columns is expected. The experimentally determined values of average large bubble

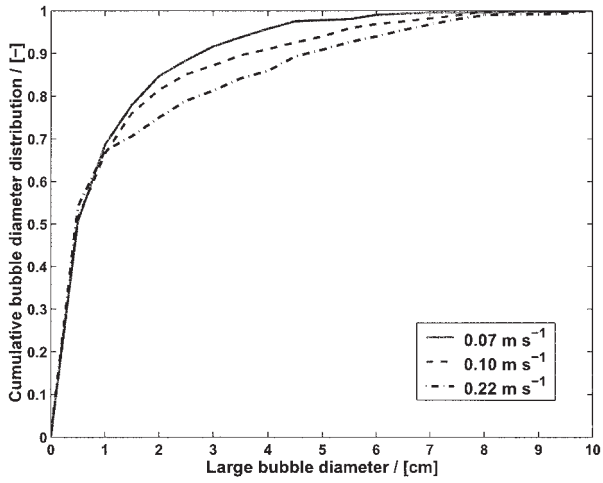

Figure 10. Bubble size distribution obtained in the 2-D SBC after processing the video images at the superficial gas velocities of 0.07, 0.10, and 0.22 m s^{-1}.

The slurry concentration was 0.056 vol/vol %.

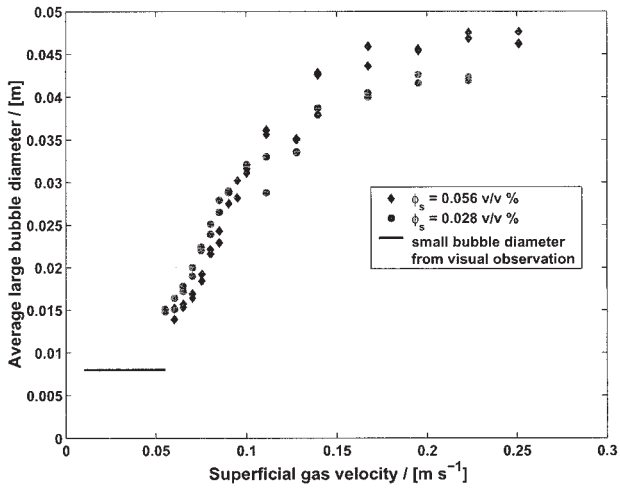

Figure 11. Average bubble size as a function of the superficial gas velocity for slurry concentrations of 0.028 and 0.056 vol/vol % in the 2-D SBC.

diameter in 2-D column are slightly higher and fall in the region of 3-D columns. Because the spread of the curves for the 2-D and 3-D column is very narrow and the powers of $d_{b,avg}$ for 2-D and 3-D columns are close to each other, the 2-D correlation is considered to be applicable for satisfactory predictions in the 3-D columns as well.

Bubble size prediction in 3-D column

For a 3-D column of 0.19-m inner diameter, the incoherent standard deviation was calculated at all the sensor positions, as shown in Figure 1b, at different gas velocities and four different slurry concentrations. The coherence between the pressure time series measured at the sparger and at the higher measurement positions was used to deconvolute the pressure time series to obtain σ_i at these four different heights. All the measurement positions were higher than the equilibrium height of 0.8 m for the 3-D column.[30] Beyond the equilibrium height, there is no bubble growth expected because of coalescence and the bubble diameter remains constant. This was confirmed by the nearly constant values of the incoherent standard deviations at all four heights. The average value of σ_i at the four measuring heights was used in Eq. 30 to estimate the average bubble diameter in the 3-D column. Krishna et al.[18] derived a semiempirical correlation to predict the diameter of large bubbles in the churn-turbulent regime in 3-D columns

$$d_{b,avg} = 0.069(u_g - u_{trans})^{0.376} \qquad \text{(m)} \qquad (31)$$

A comparison between the average large bubble diameters obtained from Eqs. 30 and 31 is given in Figure 13. The different concentration levels of carbon slurries are used to see

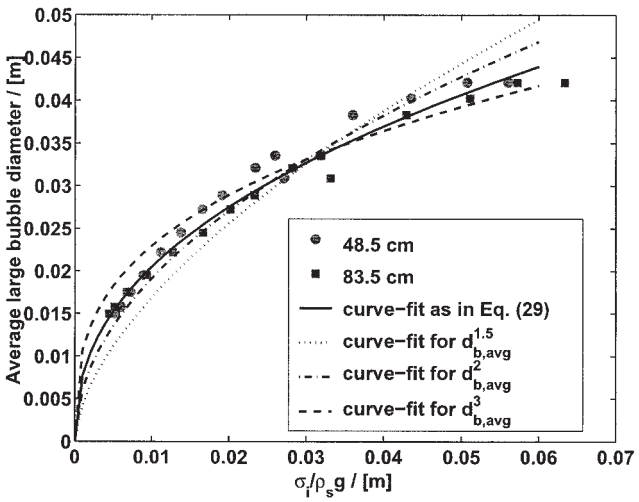

Figure 12. Comparison of the average large bubble diameter obtained from the video images with the incoherent standard deviation obtained from the spectral analysis of the pressure time series measured in the 2-D SBC at the slurry concentration of 0.028 vol/vol %.

Power-law fit of Eq. 29 and other curves for the power-law fit of power of 1.5, 2, and 3 to $d_{b,avg}$. The incoherent standard deviation was measured at the measurement height of 48.5 and 83.5 cm from the sparger.

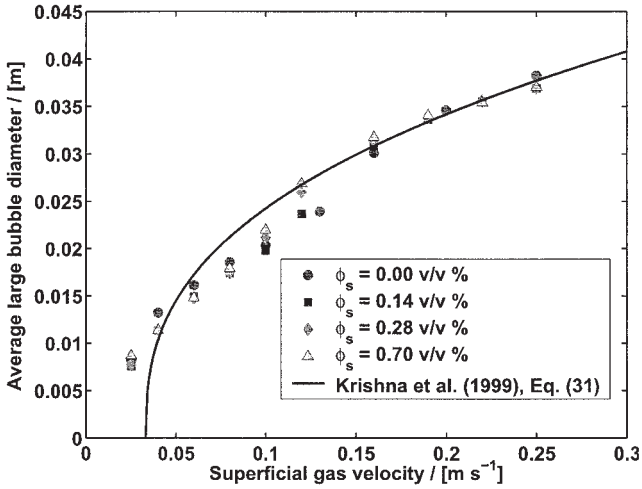

Figure 13. Comparison between the correlation for average bubble diameter (Eq. 30) and the bubble diameter model from Krishna et al.[18] in the 3-D SBC (Eq. 31).

The experimental data points are obtained by applying Eq. 30 to the measured incoherent standard deviation in the SBC.

the effect of slurry concentration on the average bubble diameter. The maximum slurry concentration used is 0.78 vol/vol %, which is not large enough to significantly change the bulk properties of the slurry. The density and effective viscosity of the slurry thus remain approximately the same and therefore there is not much difference in the predicted average bubble size in the 3-D column.

It is seen from Figure 13 that the predicted average bubble size corresponds well with Eq. 31 for higher gas velocities (>0.15 m s^{-1}). However, at the lower gas velocities, Eq. 31 deviates slightly from the predicted bubble sizes. Overall, there is a good agreement, which suggests that Eq. 30 can be satisfactorily used in (slurry) bubble columns to measure the average large bubble diameter. Because the effect of column diameter on bubble size is accounted for in the measured value of σ_i, Eq. 30 can be applied in any 3-D column to estimate the average bubble diameter. The effect of slurry concentration and of different liquids is taken into account by the slurry density ρ_s in Eq. 30. Figure 14 shows the brief algorithm to calculate the average large bubble diameter in the SBC by spectral analysis of the measured pressure fluctuations.

Conclusions

This article presents a new spectral analysis technique to measure the average large bubble diameter in the churn-turbulent regime in (slurry) bubble columns. The technique uses pressure time series measured at two locations in the column to separate the global pressure fluctuations that are present throughout the column from the local pressure fluctuations that are directly related to the passing large gas bubbles. In a 2-D slurry bubble column, a correlation is derived between the incoherent standard deviation of the pressure fluctuations and the average large bubble size as determined by video imaging. This same correlation also matches very well with the incoherent standard deviation of pressure fluctuations measured in a

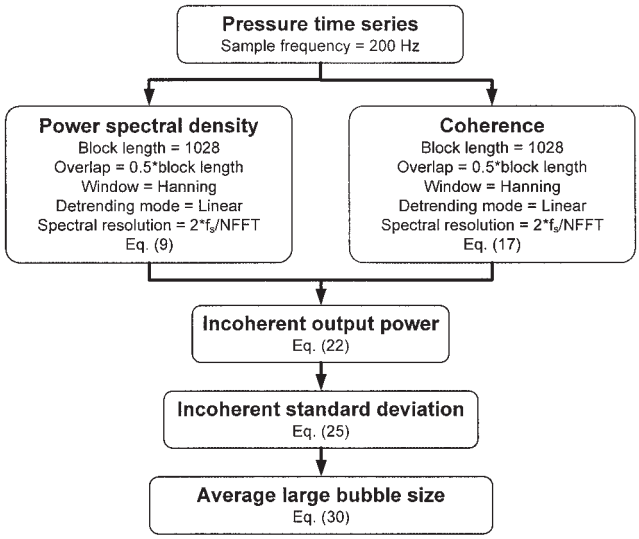

Figure 14. Summary of the algorithm to calculate the incoherent standard deviation and the average large bubble size from measured pressure time series in a slurry bubble column.

19-cm ID slurry bubble column and with the empirical bubble size correlation of Krishna et al.[18]

Acknowledgments

The authors gratefully acknowledge the Dutch Technology Foundation STW project (EPC. 5239), Akzo Nobel, DSM Research, Shell Global Solutions, and Sasol Technology Netherlands for their financial support, and Engelhard, Norit, and Promeks ASA for supplying the catalyst.

Notation

a_y = amplitude factor at position y with respect to position x, dimensionless
c = velocity of sound in gas–liquid suspension, m s^{-1}
d_b = large bubble diameter, m
$d_{b,avg}$ = average large bubble diameter, m
$E(z)$ = expectation of z, dimensions of z
$f_{b,n}$ = number of bubbles of a bubble of size $d_{b,n}$, dimensionless
$\mathcal{F}_x$ = Fourier transform at position x, Pa
g = acceleration arising from gravity, m s^{-2}
$glob$ = global sources of pressure fluctuations
loc = local sources of pressure fluctuations
N = number of bubble diameter classes, dimensionless
P = atmospheric pressure, Pa
ΔP_A = added pressure arising from volume of bubble, Pa
P_b = pressure fluctuations arising from bubbles, Pa
P_h = holdup pressure fluctuation, Pa
P_x = pressure time series at position x, Pa
r = radial coordinate, m
R_b = radius of the bubble, m
t = instantaneous time, s
Δt = time shift of global fluctuations, s
T = length of the time series, s
u_g = superficial gas velocity, m s^{-1}
u_l = axial liquid velocity, m s^{-1}
u_{trans} = regime transition velocity, m s^{-1}
v_b = rise velocity of the bubble, m s^{-1}
x = measurement position close to the sparger
y = measurement position at any height in the SBC

Greek letters

σ_c^2 = variance of global pressure fluctuations, Pa^2
σ_i = incoherent standard deviation, Pa
σ_l^2 = variance of local pressure fluctuations, Pa^2
σ_p^2 = variance of total pressure fluctuations, Pa^2
Φ_{xx} = power spectral density at position x, Pa^2 Hz^{-1}
Φ_{xy} = cross power spectral density between positions x and y, Pa^2 Hz^{-1}
γ_{xy}^2 = coherence between positions x and y, dimensionless
ρ_s = density of the slurry, kg m^{-3}
ε_g = volumetric gas holdup, dimensionless
ϕ_s = carbon particle concentration in slurry, vol/vol %
θ = angle coordinates, rad
τ_b = time required for the bubble to pass the sensor, s

Abbreviations

2-D = 2-dimensional (flat bubble column)
3-D = 3-dimensional (cylindrical column)
COP = coherent output power
CSD = cross-power spectral density
fps = frames per second
IOP = incoherent output power
PSD = power spectral density
SBC = slurry bubble column

Literature Cited

1. Joshi JB, Parasu Veera U, Prasad CV, Phanikumar DV, Deshphande NS, Thakre SS, Thorat BN. Gas hold-up structure in bubble column reactors. *PINSA*. 1998;64A:441-567.
2. Jamialahmadi M, Muller-Steinhagen H. Effect of solid particles on gas hold-up in bubble columns. *Can J Chem Eng*. 1991;69:390-393.
3. Krishna R, De Swart JWA, Ellenberger J, Martina GB, Maretto C. Gas holdup in slurry bubble columns—Effect of column diameter and slurry concentrations. *AIChE J*. 1997;43:311-316.
4. Koide K. Design parameters of bubble column reactors with and without solid suspensions. *J Chem Eng Jpn*. 1996;29:745-759.
5. Urseanu MI, Guit RPM, Stankiewicz A, van Kranenburg G, Lommen JHGM. Influence of operating pressure on the gas hold-up in bubble columns for high viscous media. *Chem Eng Sci*. 2003;58:697-704.
6. Boyer C, Duquenne AM, Wild G. Measuring techniques in gas–liquid and gas–liquid–solid reactors. *Chem Eng Sci*. 2002;57:3185-3215.
7. Larachi F, Chaouki J, Kennedy G, Dudukovic MP. Radioactive particle tracking in multiphase reactors: Principles and applications. *Non-Invasive Monitor Multiphase Flows*. 1997;335-406.
8. Dudukovic MP. Opaque multiphase flows: Experiments and modeling. *Exp Therm Fluid Sci*. 2002;26:747-761.
9. Chen J, Kemoun A, Al-Dahhan MH, Dudukovic MP, Lee DJ, Fan LS. Comparative hydrodynamics study in bubble columns using computer-automated radioactive particle tracking (CARPT)/computer tomography (CT) and particle image velocimetry. *Chem Eng Sci*. 1999;54:2199-2207.
10. Schmitz D, Mewes D. Tomographic imaging of transient multiphase flow in bubble columns. *Chem Eng J*. 2000;77:99-104.
11. Drahos J, Zahradnik J, Puncochar M, Fialova M, Bradka F. Effect of operating conditions on the characteristics of pressure fluctuations in a bubble column. *Chem Eng Process*. 1991;29:107-115.
12. Letzel HM, Schouten JC, Krishna R, van den Bleek CM. Characterisation of regimes and regime transitions in bubble columns by chaos analysis of pressure signals. *Chem Eng Sci*. 1997;52:4447-4459.
13. Glasgow LA, Erickson LE, Lee CH, Patel SA. Wall pressure fluctuations and bubble size distributions at several positions in an airlift fermentor. *Chem Eng Commun*. 1984;29:311-336.
14. Bakshi BR, Zhong H, Jiang P, Fan L-S. Analysis of flow in gas–liquid bubble columns using multi-resolution methods. *Trans IChemE*. 1995;73:608-614.
15. Vial C, Poncin S, Wild G, Midoux N. A simple method for regime identification and flow characterisation in bubble columns and airlift reactors. *Chem Eng Process*. 2001;40:135-151.
16. Lin T-J, Juang R-C, Chen Y-C, Chen C-C. Predictions of flow transition in a bubble column by chaotic time series analysis of pressure fluctuation signals. *Chem Eng Sci*. 2001;56:1057-1065.

17. Olmos E, Gentric C, Poncin S, Midoux N. Description of flow regime transitions in bubble columns via laser Doppler anemometry signals processing. *Chem Eng Sci*. 2003;58:1731-1742.
18. Krishna R, Urseanu MI, Van Baten JM, Ellenberger J. Rise velocity of a swarm of large gas bubbles in liquids. *Chem Eng Sci*. 1999;54:171-183.
19. Gluszek J, Marcinkowski R. Pressure oscillations in bubble columns. *Chem Eng J*. 1983;26:181-187.
20. Lamb H. "Surface waves." *Hydrodynamics*. New York, NY: Cambridge Univ. Press/Macmillan; 1945:Ch. IX, 364.
21. Mallock A. Absorption of sound by gas-bubbles in liquids. *Proc R Soc London* 1910;84:391.
22. De Swart JWA, Krishna R. Influence of particle concentration on the hydrodynamics of bubble column slurry reactors. *Trans IChemE*. 1995;73:308.
23. Davidson JF, Harrison D. *The Exchange between the Bubble and Particulate Phases. Fluidised Particles*. Cambridge, UK: Cambridge Univ. Press; 1963:67.
24. Davies RM, Taylor G. *Proc R Soc London Ser A Phys Sci*. 1950;200: 375-390.
25. Mudde RF, Groen JS, Van Den Akker HEA. Liquid velocity field in a bubble column: LDA experiments. *Chem Eng Sci*. 1997;52:4217-4224.
26. Johnsson F, Zijerveld RC, Schouten JC, van den Bleek CM, Leckner B. Characterization of fluidization regimes by time-series analysis of pressure fluctuations. *Int J Multiphase Flow*. 2000;26:663-715.
27. van der Schaaf J, Schouten JC, Johnsson F, van den Bleek CM. Non-intrusive determination of bubble and slug length scales in fluidized beds by decomposition of the power spectral density of pressure time series. *Int J Multiphase Flow*. 2002;28:865-880.
28. van der Schaaf J, Schouten JC, van den Bleek CM. Origin, propagation and attenuation of pressure waves in gas–solid fluidized beds. *Powder Technol*. 1998;95:220-233.
29. Kluytmans JHJ. *An Airflift Loop Redox Cycle Reactor for Alcohol Oxidations: Hydrodynamics, Mass Trasnfer and Reactor Design*. Eindhoven, The Netherlands: Technische Universiteit Eindhoven; 2003.
30. Ruzicka MC, Drahos J, Fialova M, Thomas NH. Effect of bubble column dimensions on flow regime transition. *Chem Eng Sci*. 2001; 56:6117-6124.
31. Pyle DL, Harrison D. The rising velocity of bubbles in two-dimensional fluidized beds. *Chem Eng Sci*. 1967;22:531-535.

Appendix: Translation of Davidson and Harrison Model[23] to Bubble Columns

Equation 2 (in the section "Pressure Sources in Slurry Bubble Columns") gives the correlation between pressure fluctuations of a gas bubbles in the SBC and its bubble diameter. Equation 2 is derived from the correlation proposed by Davidson and Harrison[23] for pressure fluctuation generated by a single rising gas bubble in an infinite medium in gas–solid fluidized beds. In this appendix, the complete mathematical derivation of Eq. 2 from the Davidson and Harrison[23] model is explained.

The model that Davidson and Harrison[23] derived from two-phase flow theory agrees best with the experimentally observed pressure fluctuation by a rising gas bubble in an inviscid liquid. The pressure distribution around the 2-D and 3-D gas bubble according to Davidson and Harrison is given by

$$P_b(r) = \begin{cases} -\rho_s g\left(r - \dfrac{R_b^2}{r}\right)\cos\theta & \text{2-D bubble} \\ -\rho_s g\left(r - \dfrac{R_b^3}{r^2}\right)\cos\theta & \text{3-D bubble} \end{cases} \tag{A1}$$

The pressure distribution relative to the static pressure around the spherical large gas bubble, from Eq. A1 is then given by

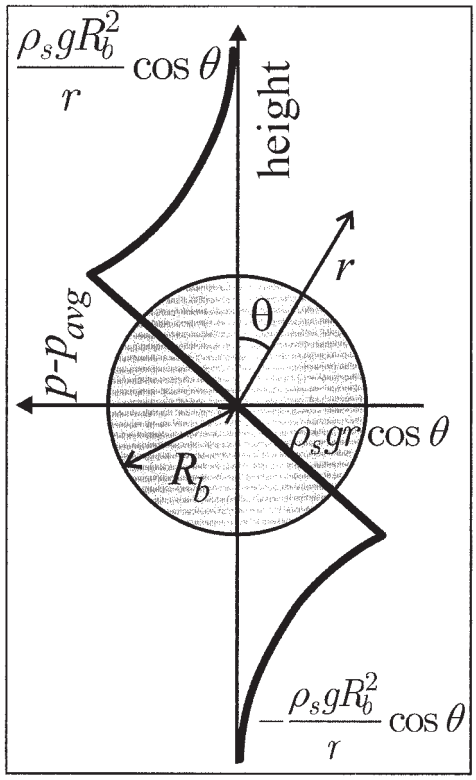

Figure A1. Radial geometry and the coordinate system used for a 2-D bubble in Eq. A2 with pressure fluctuation predicted along the center line of the gas bubble.

$$P_b(r) = \begin{cases} \rho_s g r\cos\theta & r < R_b \\ \rho_s g\dfrac{R_b^2}{r}\cos\theta & r \geq R_b \end{cases} \quad \text{2-D bubble}$$

$$P_b(r) = \begin{cases} \rho_s g r\cos\theta & r < R_b \\ \rho_s g\dfrac{R_b^3}{r^2}\cos\theta & r \geq R_b \end{cases} \quad \text{3-D bubble} \tag{A2}$$

In Figure A1 the radial geometry used in Eq. A2 is given, together with the pressure distribution along the center line of the gas bubble defined by Eq. A2. The rise velocity of a gas bubble[24,31] can be calculated with

$$v_b = \begin{cases} 0.54\sqrt{g d_b} & \text{2-D bubble} \\ 0.71\sqrt{g d_b} & \text{3-D bubble} \end{cases} \tag{A3}$$

The radial coordinates in Figure A1 are converted into rectangular coordinates as in Figure A2. In Figure A2, the 2-D gas bubble is assumed to be stationary, whereas the liquid is moving downward with the velocity equal to the rise velocity of the bubble, v_b. A pressure probe measuring the pressure profile around the bubble, having coordinates (x_p, z_p), is also assumed to move downward with velocity v_b. At $t = 0$, the pressure probe reaches the height of the center of the bubble (that is, for $\theta = 90°$, $r = x_p$ and $z_p = 0$). The changed coordinates of the pressure probe from (r, θ) to (x_p, z_p) are given as

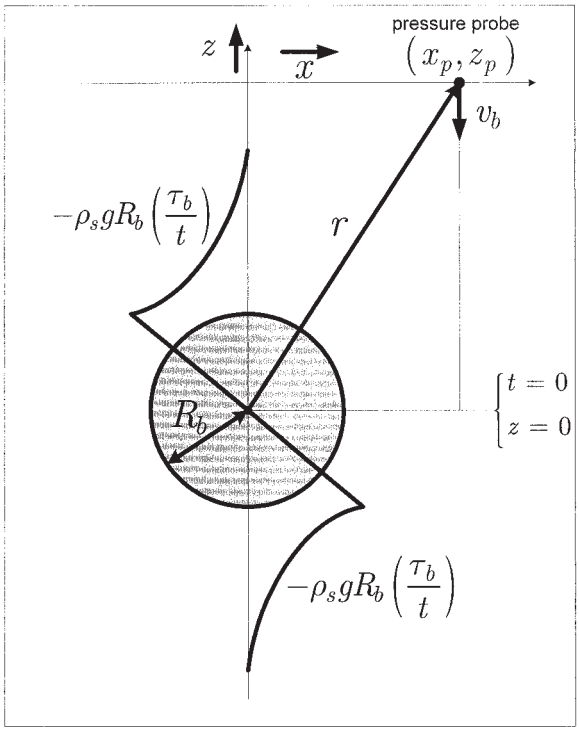

Figure A2. Rectangular coordinate system used for a 2-D bubble with pressure fluctuation along the center line of the gas bubble.

$$z_p = r\cos\theta = -v_b t$$

$$x_p = r\sin\theta$$

$$r^2 = z_p^2 + x_p^2 \tag{A4}$$

For ease of calculations, we consider the centerline of the bubble, at $\theta = 0$, $r = v_b t$. Using this and Eq. A3 in Eq. A2, the pressure fluctuation as a function of time for a 2-D gas bubble is obtained:

$$P_b(t) = \begin{cases} -\rho_s g R_b\left(\dfrac{\tau_b}{t}\right) & t \notin [-\tau_b, \tau_b] \\ -\rho_s g R_b\left(\dfrac{t}{\tau_b}\right) & t \in [-\tau_b, \tau_b] \end{cases} \tag{A5}$$

where the top of the gas bubble reaches the measurement position at $t = -\tau_b = R_b\cos\theta/v_b$. A similar more complex expression is obtained for $\theta > 0$, which we will not discuss here.

In addition to the pressure fluctuation caused by the pressure distribution around the gas bubble, another type of pressure fluctuation is generated when the gas bubble passes the measurement position. When a gas bubble is formed below the measurement position, the liquid height increases and more liquid is present above the measurement position.

Consequently, the static pressure increases at the measurement position. When the bubble passes the measurement position, the static pressure returns to the original value. The added pressure resulting from the presence of a gas bubble below the measurement position is given by (R_c is half of the column width)

$$\Delta P_A = 4\rho_s g R_b\left(\frac{R_b}{R_c}\right) \tag{A6}$$

When the top of the bubble reaches the measurement position at time $t' = 0$, the amount of added liquid above the measurement position starts to decrease in time. The resulting pressure fluctuation is given by

$$P_b(t') = \Delta P_A - \rho_s g R_b\left(\frac{R_b}{R_c}\right)\left(\frac{t'}{\tau_b}\right)\left(1 + \frac{1}{2}\frac{t'}{\tau_b}\right) \tag{A7}$$

if the gas bubble is assumed circular. At time $t' = 2\tau_b$, the static pressure will have returned to its original value. The pressure fluctuation given by Eq. A7 is presented in Figure A3 for $R_b = 0.025$ m, $R_b/R_c = 1.667$, and $\tau_b = 0.14$ s.

The pressure fluctuation predicted by Davidson and Harrison can be corrected for this decrease in the amount of liquid mass present above the measurement position with Eq. A7, which results in

$$P_b(t) = \begin{cases} \rho_s g R_b\left(\dfrac{\tau_b}{t}\right) + \Delta P_A & t < -\tau_b \\ \Delta P_A - \rho_s g R_b\left[\dfrac{t}{\tau_b} + \cdots + \left(\dfrac{R_b}{R_c}\right)\left(\dfrac{t'}{\tau_b}\right)\left(1 + \dfrac{1}{2}\dfrac{t'}{\tau_b}\right)\right] & -\tau_b \le t < \tau_b \\ -\rho_s g R_b\left(\dfrac{\tau_b}{t}\right) & t \ge \tau_b \end{cases} \tag{A8}$$

The pressure fluctuation given by Eq. A8 is also shown in Figure A3. The experimentally observed shape of the pressure fluctuation by a rising gas bubble in the single gas pulse experiments depicted in Figure 2 corresponds well to the curves predicted by Eq. A8. Experimentally, the added pressure effect appears more significant, and the predicted pressure increase in front of the bubble also seems to be significant, as seen from Figure A3. Additionally, the pressure recovery behind the bubble is more pronounced.

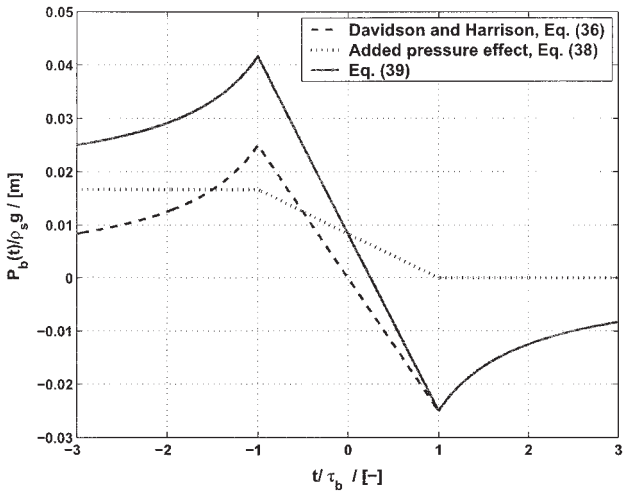

Figure A3. Pressure fluctuation predicted by Eqs. A5, A7, and A8.

Equation A8 can be further simplified to

$$P_b(t) \propto \rho_s g \frac{d_b^2}{v_b t} \qquad \text{2-D bubble}$$

$$P_b(t) \propto \rho_s g \frac{d_b^3}{v_b^2 t^2} \qquad \text{3-D bubble} \qquad \text{(A9)}$$

Here it is seen that the pressure fluctuation by a 2-D gas bubble is proportional to the square of the bubble diameter. Extending this analysis for a 3-D bubble it is found that the pressure fluctuation is proportional to the cube of the bubble diameter, as in Eq. A9.

Manuscript received Jun. 9, 2004, and revision received Oct. 27, 2004.